Chapter 4
Microstructural Characterization

This chapter illustrates the detailed microstructural characterization of the Mg-5.0Al-2.0Ca-0.3Mn (wt.%) (AXM520) alloy and nanocomposites. The microstructural characterization was carried out using X-ray Diffraction (XRD), Optical Microscopy (OM), Scanning Electron Microscopy (SEM), and Transmission Electron Microscopy (TEM). The XRD detected the various phases present in the microstructure of the alloy and nanocomposites. The representative micrographs for all the alloys were taken using OM and SEM. The composition of the phases was analyzed by the Energy-Dispersive X-ray Spectroscopy (EDS) attached to the SEM and TEM. The major outcomes of the present chapter are summarised at the end.

4.1 X-ray diffraction analysis

The ambient temperature solid solubilities of Ca and Mn in Mg are negligible. Therefore, the formation of Ca- and Mn-rich intermetallic phases in the AXM520 alloy is expected. Figure 4.1(a to c) presents the X-ray diffraction patterns obtained from the alloy and nanocomposites (NCs). Analysis of the XRD patterns confirmed the existence of the Mg solid solution (i.e., α-Mg) and $(Mg,Al)_2Ca$ (C36) (M. P. 988 K) phases in the alloy and NCs. The magnified view of the XRD patterns of the AXM520 alloy and NC3.0SiC (representative picture of the NCs) in the 2θ range from 30 to 50 are presented in Figure 4.1(b). The XRD peaks obtained from the C36 phase are shown. Thus, the intensity of the XRD pattern for the C36 phase is reasonably prominent, and it is as per the pattern reported by Zubair et al. [58] for the same phase. The Al_8Mn_5 phase was also observed in the AXM520 alloy and NC3.0SiC. As expected, the presence of the SiC phase was confirmed in the XRD pattern of the NC3.0SiC. The β-$Mg_{17}Al_{12}$ (A12) (M. P. 733 K) phase was suppressed in the alloy and NCs employed in the current investigation, and the suppression was attributed to the chosen Ca/Al ratio of 0.40. Similar results were also observed by other researchers [13,14]. Ninomiya et al. [15] concluded that the occurrence of the Al_2Ca (C15) phase (M. P. 1352 K) suppressed β phase in the Mg-Al-Ca alloy containing a ratio of Ca to Al of 0.11. They also observed that further incorporation of

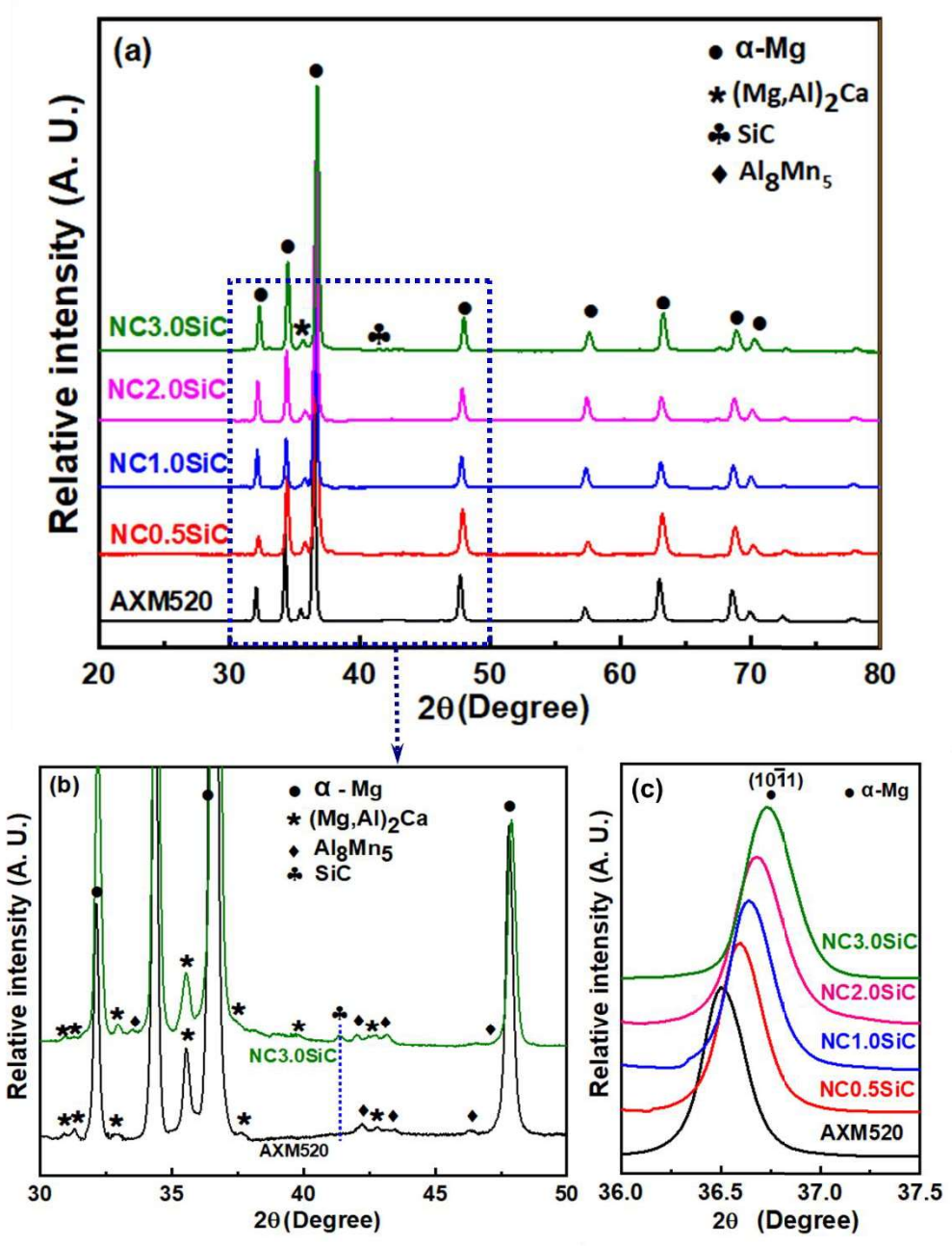

Figure 4.1 (a) XRD patterns obtained from the as-cast AXM520 alloy and all the nanocomposites; (b) magnified view of the XRD patterns obtained from the AXM520 alloy and NC3.0SiC in the 2θ range from 30 to 50 °; and (c) magnified view of the 2θ range from 36.0 to 37.5 ° confirming the shift of the high-intensity peak of the α-Mg phase.

Ca (Ca/Al ≥ 0.83) in the Mg-Al-based alloys encouraged the formation of the Mg_2Ca (C14) (M. P. 988 K) phase along with the Al_2Ca (C15) phase. Table 4.1 summarises the phases previously reported [56,59,86-89] in the Mg-Al-Ca-Mn alloys with a Ca/Al fraction close to that of the present investigation, i.e., Ca/Al = 0.40. The presence of the $(Mg,Al)_2Ca$ (C36) phase is evident in all the alloys. The presence of the Al_8Mn_5 phase in the Mg-Al-Ca-Mn alloys was reported by other researchers as well [59,88]. No peaks corresponding to alumosilicate and Mg_2Si were detected in the XRD patterns, confirming the absence of reaction products. The enlarged view of the $(10\bar{1}1)$ peaks corresponds to the α-Mg phase present in the alloy, and NCs are shown in Figure 4.1(c). It is evident that the high-intensity peak of the α-Mg phase shifted towards the right of the XRD patterns as the concentration of the SiC_{np} increased in the AXM520 alloy. The presence of SiC_{np} hinders solid rejection during solidification of the NCs by encapsulating the solid phase [90,91]. In the present investigation, Al rejection from the α-Mg phase nuclei was hindered owing to the presence of the SiC_{np}, which resulted in the enrichment of the α-Mg phase. The atomic radii of Mg and Al are 150 and 125 pm, respectively [92]. Therefore, the lattice contraction of the α-Mg phase took place, which contributed to the right shift of the $(10\bar{1}1)$ peak.

Table 4.1 Summary of the phases formed in the Mg-Al-Ca-Mn alloys reported in the literature.

Alloy	Composition (wt.%)				Phases present in as-cast condition	Ref.
	Al	Ca	Mn	Ca/Al		
AXM5203	4.50	1.90	0.27	0.42	α-Mg, C36	[86]
AXM523	5.11	2.33	0.33	0.44	α-Mg, C15, C36	[87]
AXM520	5.00	2.00	0.40	0.40	α-Mg, C36, Al_8Mn_5	[88]
AXM63011	6.10	3.20	0.11	0.52	α-Mg, C36, C14	[89]
AXM6305	6.00	3.20	0.46	0.52		
AXM4204	4.00	2.00	0.40	0.50	α-Mg, C36	[56]
AXM7303	6.90	3.30	0.30	0.47	α-Mg, C36, Al_8Mn_5	[59]

4.2 Optical and SEM micrographs

Figure 4.2(a to e) displays the optical images of the alloy and NCs with the corresponding grain size distribution. The continuous network of the dark $(Mg,Al)_2Ca$ (C36) phase was distributed along the interdendritic regions in the AXM520 alloy. The grain size of all the NCs was smaller

compared to the AXM520 allo, as estimated by the linear intercept method, summarized in Table 4.2. The grain size of the NCs reduced as the concentration of the SiC_{np} increased in the AXM520 alloy, and the same decreased by 36.8% in the NC3.0SiC. The grain refinement in the NCs was owing to the heterogeneous nucleation of α-Mg on the nanoparticles during solidification. The phenomenon of grain refinement in Mg alloy following the nanoparticle additions was reported previously as well [30].

Table 4.2 The calculated grain size, volume fraction, and fractal dimension of the C36 phase in the alloy and nanocomposites.

Alloy/ Nanocomposite	Grain size (µm)	Volume fraction of C36 phase (%)	Fractal dimension (D_f) of C36 phase
AXM520	52.5±12.1	17.41	1.58
NC0.5SiC	48.1±10.1	15.35	1.38
NC1.0SiC	43.2±11.1	13.82	1.29
NC2.0SiC	37.9±6.2	12.02	1.12
NC3.0SiC	33.2±6.3	11.51	1.10

The SEM image of the alloy is provided in Figure 4.3(a), and its enlarged view is displayed in Figure 4.3(b). Three different contrasts were observed in the micrograph. The dark grey and grey contrasts were identified as the α-Mg and C36 phases, respectively, and the bright spots correspond to the Al_8Mn_5 phase. The X-ray elemental mapping for Mg, Al, Ca, and Mn obtained from Figure 4.3(b) is displayed in Figure 4.3(c). The existence of Mg, Mg-Al-Ca, and Al-Mn-rich phases was confirmed in the micrograph of the AXM520 alloy. Another magnified view of the AXM520 alloy is presented in Figure 4.3(d), and the elemental analyses were performed in it. The EDS spectra from inside the grain (Spot 1) demonstrated the composition of Mg-2.6Al-0.3Ca (at.%), confirming α-Mg. The EDS spectra obtained from the lamellar phase (Spot 2) display the presence of Mg-28.5Al-14.9Ca (at.%), confirming the C36 phase. Li et al. [56] too reported a similar composition of C36 phase in the AXM alloy. Further, EDS spectra taken from the blocky phase (Spot 3) were identified as the Al_8Mn_5 phase with the composition of Mg-47.6Al-43.3Mn (at.%). A similar composition of the Al_8Mn_5 phase in the AXM alloys was stated by other researchers as well [59,88].

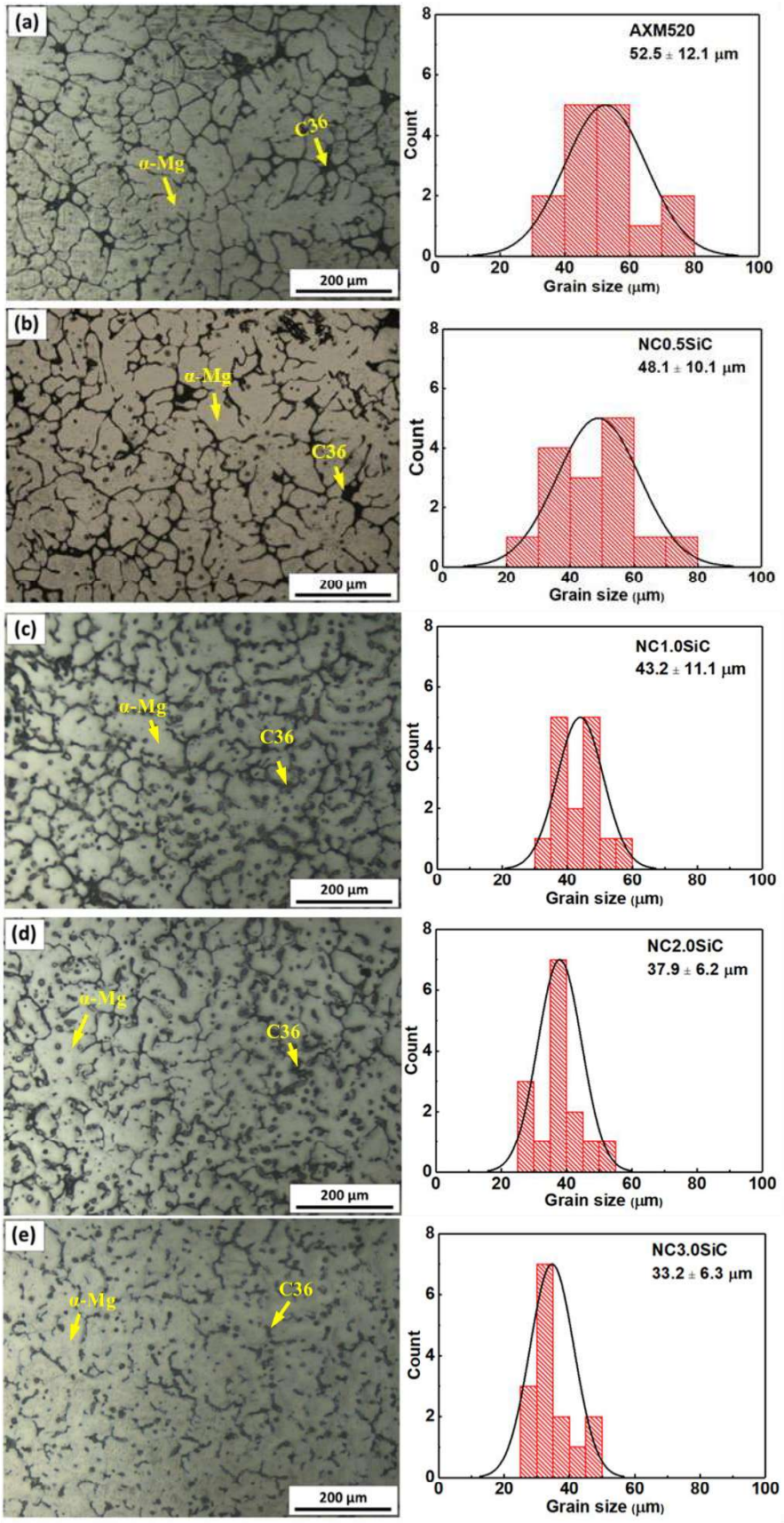

Figure 4.2 Optical micrographs with the corresponding grain size distribution of the (a) AXM520 alloy, (b) NC0.5SiC, (c) NC1.0SiC, (d) NC2.0SiC, and (e) NC3.0SiC nanocomposites.

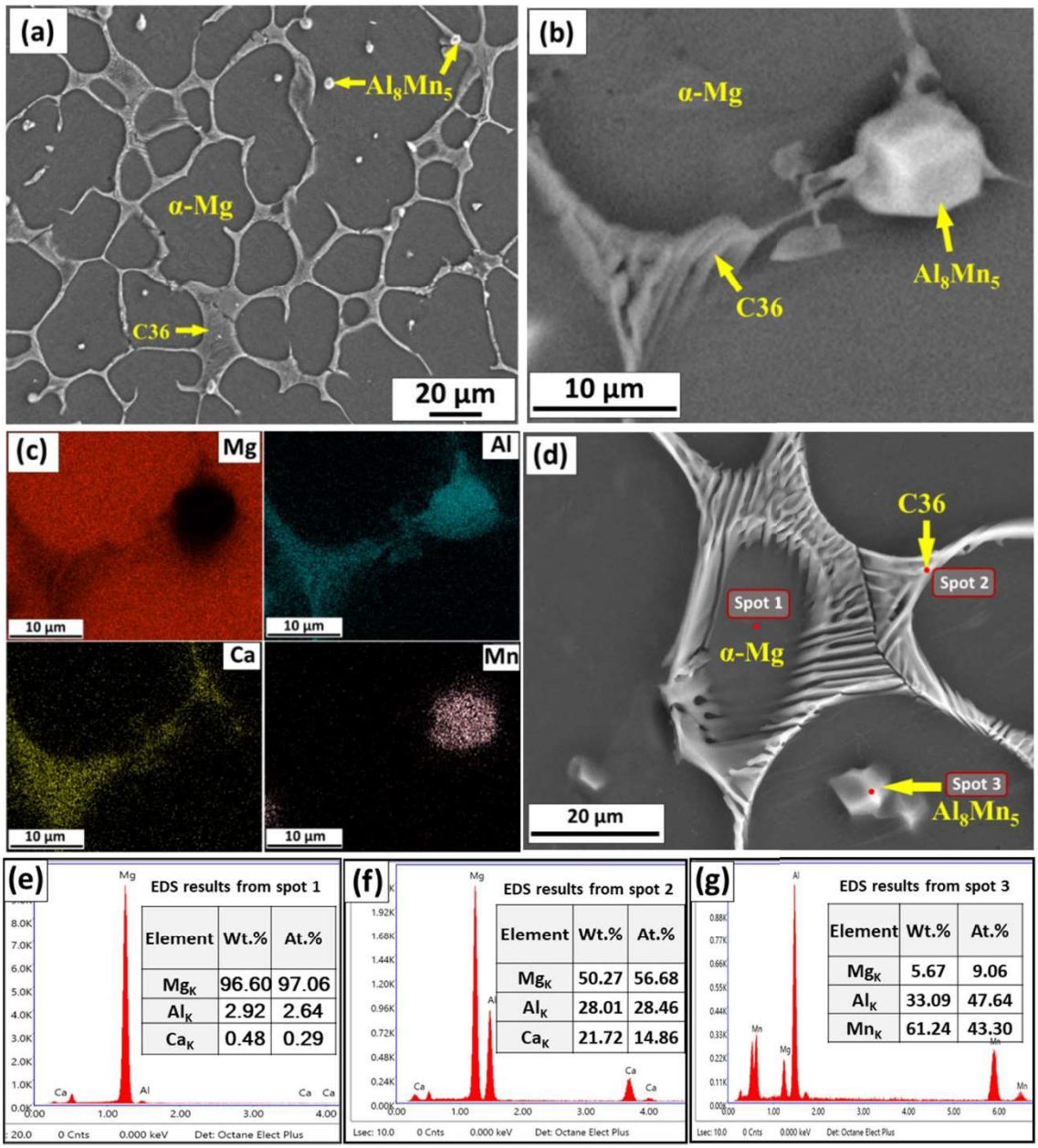

Figure 4.3 (a) SEM micrograph of as-cast AXM520 alloy; (b) a magnified view of 'a'; (c) X-ray elemental mapping of Mg, Al, Ca and Mn corresponding to 'b'; (d) another magnified view of 'a' indicating the regions of EDS analysis; EDS spectra taken from (e) spot 1 confirming α-Mg phase, (f) spot 2 confirming C36 phase, and (g) spot 3 confirming Al_8Mn_5 phase.

Figure 4.4(a to d) reveals the SEM micrographs of the NCs. The as-cast microstructures of all the NCs too consist of α-Mg phase, a eutectic of α-Mg and $(Mg,Al)_2Ca$ (C36) phases and a Al_8Mn_5 phase. Additionally, the SiC phase is also present in the NCs. The continuous network of the C36 phase in the NCs is fragmented and becomes discontinuous as the concentration of the SiC_{np} increases in the NCs. The amount of the C36 phase decreased with an increase in the concentration of the SiC_{np} in the NCs. The presence of the SiC_{np} in the matrix dissolved a fraction of the C36 phase and broke down its continuous network. The reason behind the reduction of the C36 phase has been discussed in section 4.3. A similar observation was also made by Huang et al. [93]. The β-$Mg_{17}Al_{12}$ phase in their investigation dissolved in α-Mg with increased concentration of the dispersed SiC and Al_2O_3 phases. Moheimani et al. [94] also observed that incorporating the AIN nanoparticles in EV31 alloy reduced the amount of secondary Mg_3RE in the nanocomposite. Ganguly and Mondal [30] also concluded that the extent of β-$Mg_{17}Al_{12}$ phase diminished with increase in SiC nanoparticles concentration in the AZ91-Ca-Sb-alloy-based nanocomposites.

4.3 Fractal analysis of SEM micrographs

The fractal analyses were carried out to study the connectivity of the C36 phase of the as-cast alloy and NCs. The microstructures of the AXM520, NC0.5SiC, and NC3.0SiC at a fixed magnification are presented in Figure 4.5(a to c). The maximum connectivity of the C36 phase was in the AXM520 alloy. The connectivity of the C36 phase decreased as the concentration of the nanoparticles increased in the NCs. Furthermore, the network of the C36 phase surrounding the α-Mg phase disappeared gradually with the increase in the SiC_{np} content, and it was the lowest in the NC3.0SiC, as shown in Figure 4.5(c). For better clarity, the connectivity of the secondary phase network was further quantified in terms of fractal dimension (D_f) and was plotted in Figure 4.5(d to f). The results show that the slopes of the curves decreased as the concentration of the nanoparticles increased in the NCs. The slope was the maximum (i.e., 1.58) corresponding to AXM520 alloy, and the same was the minimum (i.e., 1.10) in NC3.0SiC. The estimated content of the C36 phase in both the alloy and NCs, and corresponding fractal dimensions are presented in Table 4.2. For a well-developed secondary phase network, the value of D_f should be two, whereas it is one for the fragmented network [35]. Based on the values of D_f presented in Table 4.2, it is evident that the connectivity of the grain boundary phase decreased as the concentration of the SiC_{np} increased in the NCs.

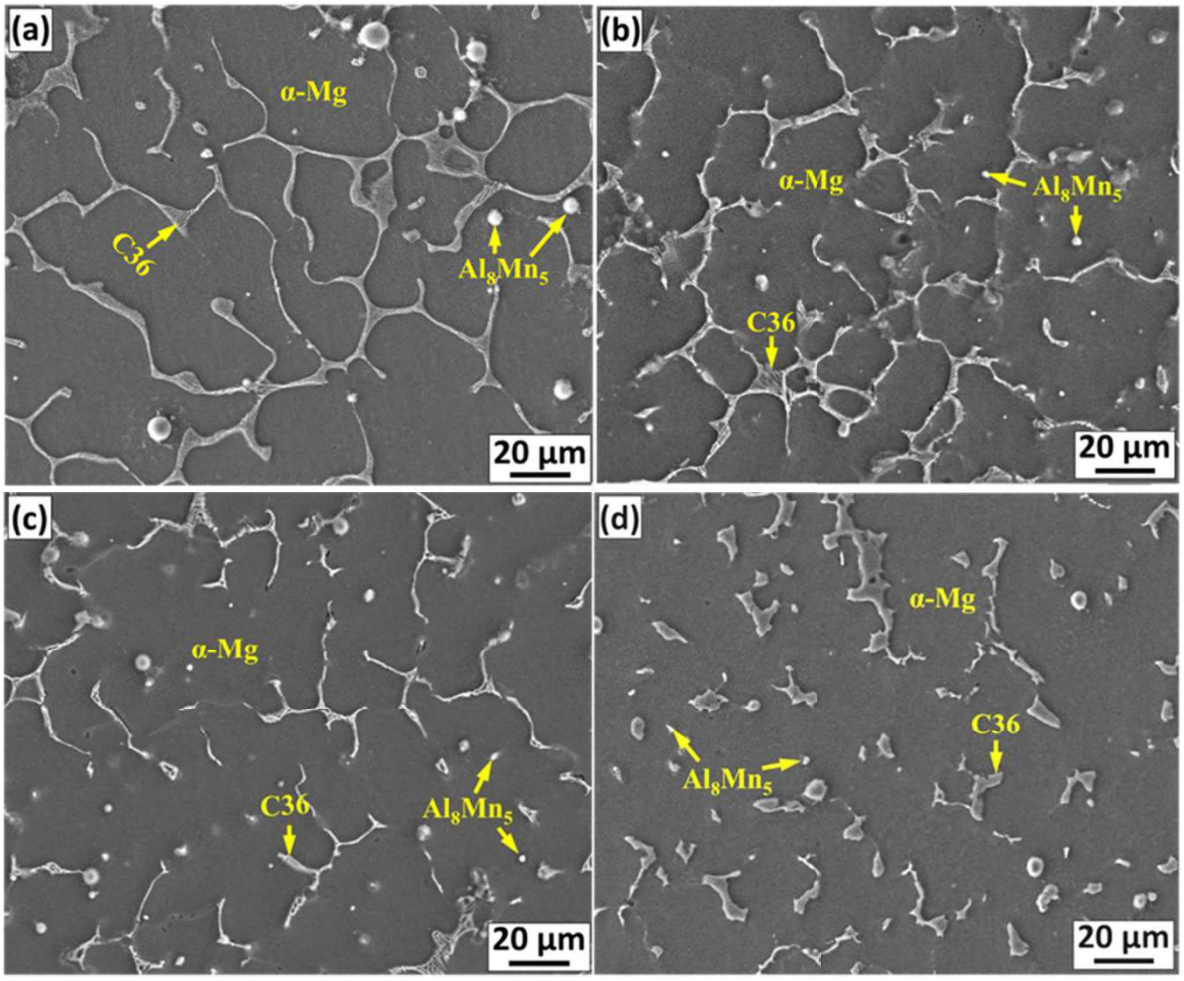

Figure 4.4 SEM micrographs of the as-cast (a) NC0.5SiC, (b) NC1.0SiC, (c) NC2.0SiC, and (d) NC3.0SiC nanocomposites.

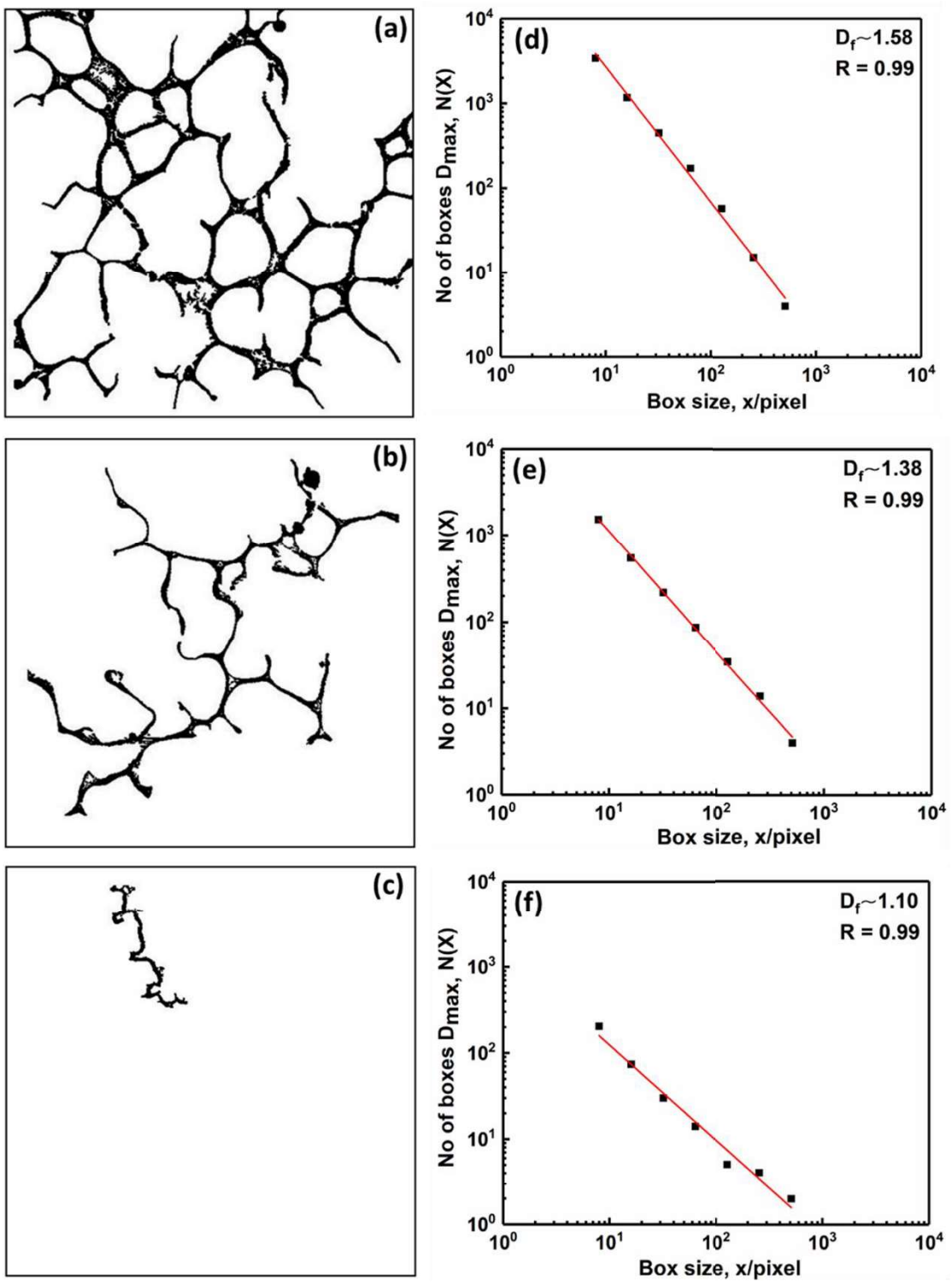

Figure 4.5 Fractal analyses of the (a) AXM520, (b) NC0.5SiC, and (c) NC3.0SiC exhibiting the maximum connected C36 phase extracted from the respective binary SEM images; and (d) to (f) exhibit the fractal dimension (D_f) plots obtained from the respective images fractal dimension (D_f) plots obtained from the respective images from 'a' to 'c'.

During solidification, the alloying elements Al and Ca were directed towards the boundaries between the solid and liquid phases, and accordingly, the secondary phase formation took place along the grain boundaries of the alloy [56]. Suzuki et al. [16] reported that the liquid (L) → α-Mg + $(Mg,Al)_2Ca$ (C36) reaction took place at 807 K and a Ca/Al fraction of 0.52. They also mentioned that for the Ca/Al fraction beyond 0.52, the eutectic reaction: liquid (L) → α-Mg + Mg_2Ca (C14) + C36 took place. The Ca/Al fraction in the present investigation is restricted below 0.50, and accordingly, the formation of the C14 was not observed in the AXM520 alloy. The role of the nanoparticles during solidification, i.e., the occurrence of the α-Mg as well as secondary C36 phases in the AXM520 alloy, can be understood from the reported literature on the nanocomposites. Xu et al. [95] in their work revealed that the nanoparticles were engulfed by the growing dendrites or pushed towards the liquid phase during solidification. Chen et al. [90] showed that the nanoparticles acted as a physical barrier during the growth of the solid phase. Wang et al. [91] showed that the presence of nanoparticles during solidification greatly impeded the solute rejection from the solid phase. Guo et al. [96] too showed that as the local concentration of nanoparticles increased in the liquid melt, the diffusion of the major solute particles were hindered during solidification. They also mentioned that the viscosity of the liquid melt increased in the presence of nanoparticles, resulting in a decrease in the solute diffusion process. Thus, during the solidification of the NCs in the present investigation, one or more phenomena might have occurred, resulting in the morphological change and reduction in the fraction of the secondary C36 phase in the NCs. However, it is impossible to identify and isolate the individual mechanism responsible for the decrease of amount of the C36 phase. This requires a comprehensive examination of the solidification characteristics of the alloy and NCs, which is not within the scope of the current study.

4.4 TEM analysis

Figure 4.6(a) shows the TEM bright-field (BF) image of the intermetallic phase in the AXM520 alloy. The image taken from the eutectic region exhibits the presence of the alternate layers of the α-Mg phase with bright contrast and an unknown phase with dark contrast. The eutectic was distributed across several microns along the width. The SAED pattern acquired from the dark portion of the eutectic shown in Figure 4.6(b) confirms the $(Mg,Al)_2Ca$ phase with a double hexagonal crystallographic structure (C36). Thus, the microstructure of the AXM520 alloy comprises α-Mg grains as well as the eutectic of α-Mg and $(Mg,Al)_2Ca$ (C36) phases

along grain boundaries and triple points. The careful analysis of the SAED pattern confirms the following orientation relationships between α-Mg and C36 phases.

$$(0001)_{\alpha\text{-Mg}} \,||\, (0001)_{C36}\ ,\ [10\bar{1}0]_{\alpha\text{-Mg}} \,||\, [11\bar{2}0]_{C36}$$

A similar orientation relationship was reported by Luo et al. in their work on Mg-5Al-3Ca alloy [97]. The lattice parameters of the α-Mg and C36 phases were also calculated from the SAED pattern. The lattice parameter value for α-Mg was approximately a = 3.19 Å and c = 5.23 Å, and the same for the C36 phase was a = 5.92 Å and c = 9.87 Å. Figure 4.6(c) shows the BF micrograph acquired from the intermetallic phase observed in the NC3.0SiC, and the analysis of its SAED pattern in Figure 4.6(d) confirms existence of C36 phase in the α-Mg matrix of the NCs as well. The precipitate has an irregular shape with an average width of 1.58±0.6 µm. The BF image and its SAED pattern taken from the matrix of the NC2.0SiC shown in Figure 4.6(e and f), exhibits an almost homogeneous distribution of SiC_{np} in α-Mg matrix. Figure 4.6(g) reveals the agglomeration of the nanoparticles in the matrix of the NC3.0SiC. The corresponding SAED pattern shown in Figure 4.6(h) with ring-like appearance confirms the presence of the SiC phase, and the dot pattern was from the primary Mg phase. The high-resolution (HR)-TEM image of the SiC_{np} present in the α-Mg phase is shown in Figure 4.7(a). The First Fourier Transformation (FFT) of Figure 4.7(a) confirms that the observed fringes correspond to the (002) plane of the SiC phase, is shown in Figure 4.7(b). The SiC_{np} present in the grain interior resulted from the engulfment of the SiC_{np} phase by the solid-liquid interface during the solidification of the melt. Figure 4.7(c and d) exhibits a TEM-BF micrograph of the grain boundary region, and the corresponding SAED with ring pattern. The analysis of the SAED pattern confirms the coexistence of the C36 and SiC_{np} phases at the grain boundary region of NC3.0SiC nanocomposites. Fractions of the added SiC_{np} were pushed along the solid-liquid interface and decorated along the boundaries of the C36 phase.

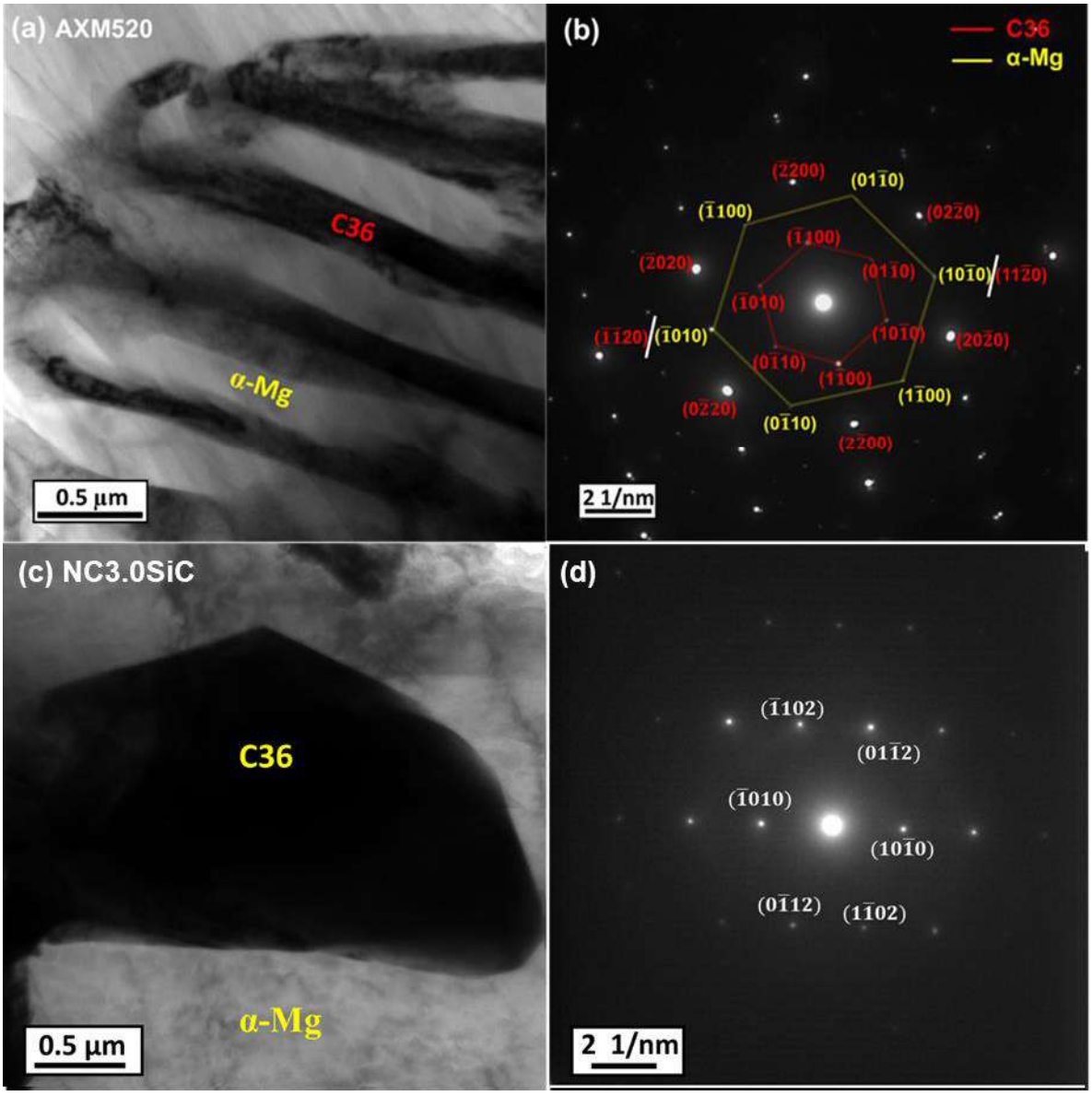

Figure continued to next page

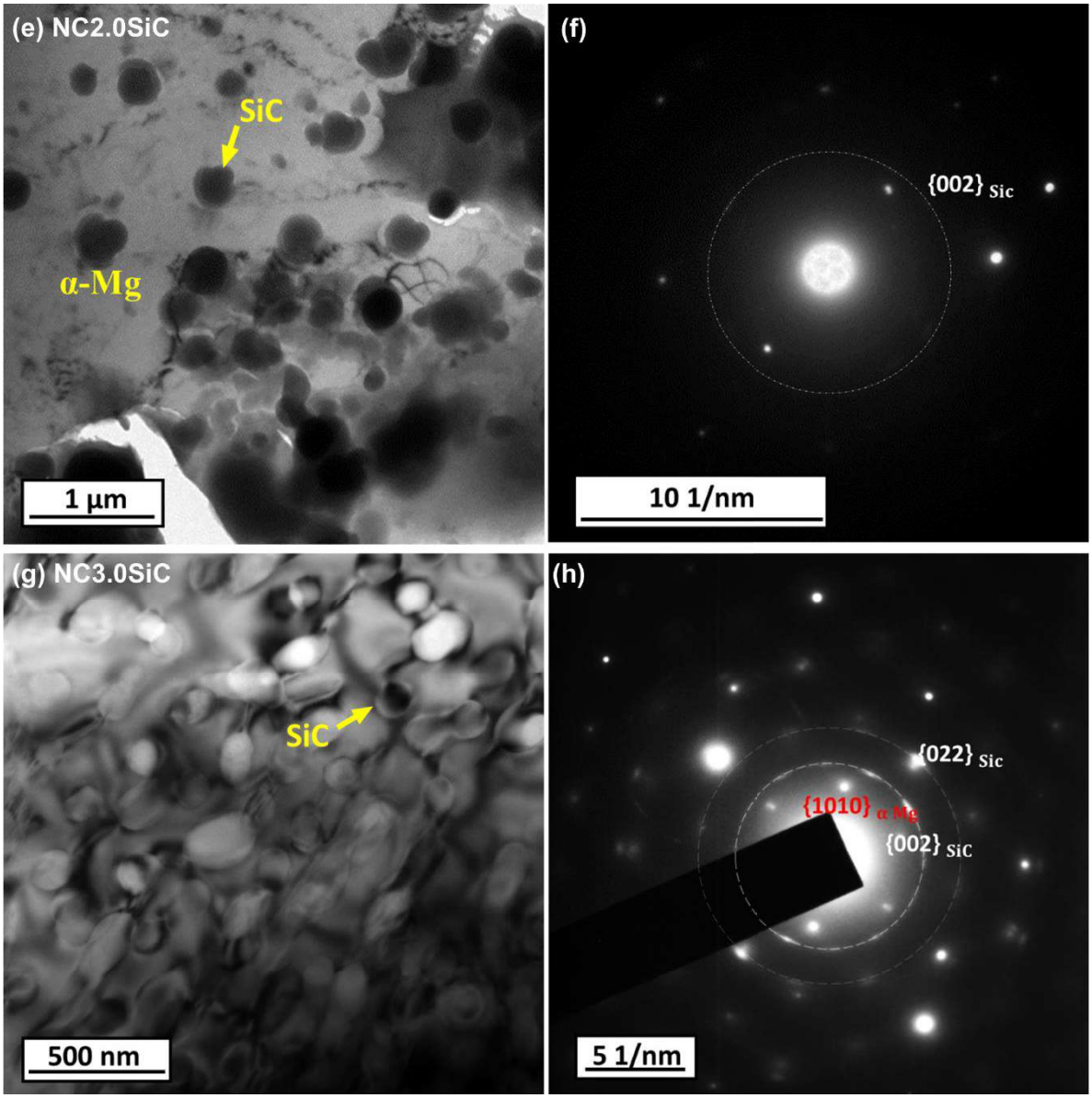

Figure 4.6 (a) TEM BF image taken from the C36 phase of AXM520 alloy, and (b) SAED pattern corresponding to 'a' with beam direction B = [0001]; (c) TEM BF image taken from the C36 phase of NC3.0SiC, and (d) SAED pattern corresponding to 'c' with beam direction B =[$\bar{2}4\bar{2}3$]; (e) TEM BF image taken from the matrix of NC2.0SiC exhibiting the distribution of SiC nanoparticles, and (f) SAED pattern corresponding to 'e'; (g) TEM BF image taken from the matrix of NC3.0SiC exhibiting the agglomeration of SiC nanoparticles, and (h) SAED pattern corresponding to 'g'.

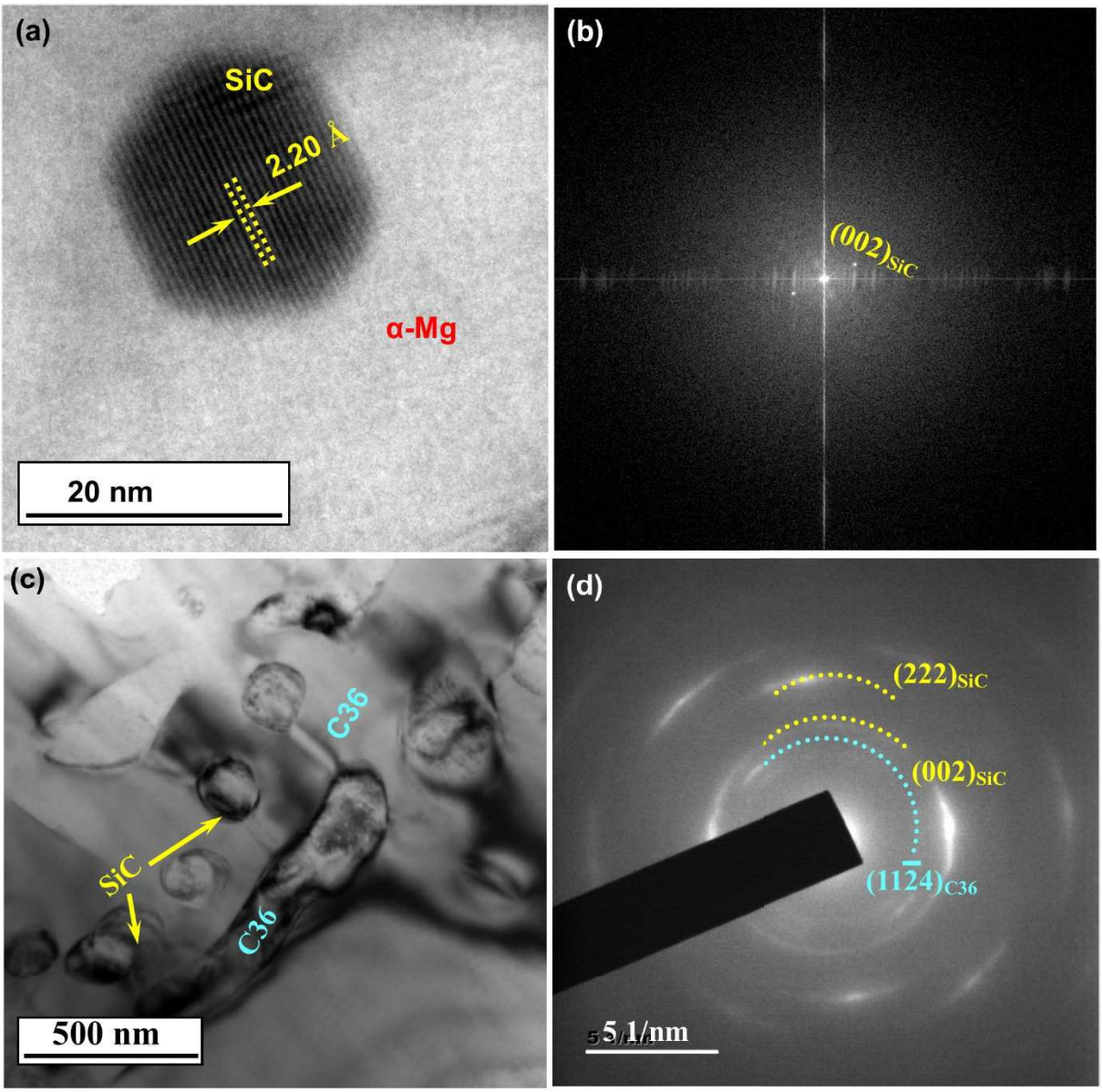

Figure 4.7 (a) HR-TEM image of the SiC_{np} present in α-Mg of NC3.0SiC; (b) FFT corresponding to 'a'; (c) distribution of SiC_{np} close to the C36 phase at the intergranular region of the NC3.0SiC; and (d) SAED pattern corresponding to 'c'

4.5 Summary of chapter 4

In this chapter, the detailed microstructural characterization of the squeeze-cast Mg-5.0Al-2.0Ca-0.3Mn (AXM520) alloy and its nanocomposites dispersed with 0.5, 1.0, 2.0, and 3.0 (wt.%) of SiC_{np} has been presented. The nanocomposites (NCs) were abbreviated as NC0.5SiC, NC1.0SiC, NC2.0SiC and NC3.0SiC. The major findings from the current chapter are summarized below.

i. The microstructures of AXM520 alloy and NCs consist of a primary solid solution (α-Mg), a eutectic of α-Mg and $(Mg,Al)_2Ca$ (C36) phases, and an Al_8Mn_5 phase. Additionally, the SiC phase was also present in the NCs.

ii. The grain size of the NCs reduced as the concentration of the SiC_{np} increased in the AXM520 alloy, and the same decreased by 36.8% in the NC3.0SiC.

iii. The C36 phase formed a continuous network in the AXM520 alloy. However, the same in the NCs was fragmented and became discontinuous with the increase in the fraction of the SiC_{np}. Thus, the C36 phase was the most fragmented in the NC3.0SiC.

iv. The α-Mg and C36 phase present in the AXM520 alloy exhibited an orientation relationship of $(0001)_{\alpha\text{-Mg}} \,||\, (0001)_{C36}$, $[10\bar{1}0]_{\alpha\text{-Mg}} \,||\, [11\bar{2}0]_{C36.}$ The lattice parameter values for the α-Mg and C36 phases were found to be a = 3.19 Å, c = 5.23 Å, and a = 5.92 Å, c = 9.87 Å, respectively.